ADVANCED ENERGY & SUSTAINABILITY RESEARCH
www.advenergysustres.com

Tungsten Carbide Nanoparticles Embedded in Carbon Nanofoam Composites for Efficient Electrocatalytic Hydrogen Evolution

Stefanos Chaitoglou, Subrata Ghosh,* Rogelio Ospina, Yang Ma, Roger Amade-Rovira, Carlo S. Casari, and Enric Bertran-Serra*

Efficient hydrogen evolution via water electrolysis requires the use of advanced electrocatalysts. To date, the preparation of support composites with a high load of catalytically active species remains a critical challenge. This study demonstrates the effectiveness of simultaneous laser ablation of two targets—a transition metal target and a graphite target—for synthesizing 3D nanoporous carbon/transition metal carbide composites. By varying the laser ablation position followed by postannealing treatment, the stoichiometry of the resulting composites can be precisely controlled. Morphological analysis reveals the homogeneous embedding of transition metals within a carbon foam, characterized by a dense network of nanoparticles. Annealing-induced carburization and crystallization significantly enhance the electrocatalytic performance for hydrogen evolution. The optimized nanostructures show impressive results, with low overpotential values (−278 mV at 10 mA cm^{-2}) and remarkable stability over extended durations (up to 10 h) under high current densities (up to 580 mA cm^{-2}). These findings highlight the potential for creating highly homogeneous carbon-supported metallic nanoporous composites suitable for energy sector applications and other technological uses.

1. Introduction

The quest for acquisition of green, carbon-neutral, energy is one of the major challenges that our society needs to solve to cope with the intense electrification, especially in heavy industry.[1] Undoubtedly, renewable and abundant energy sources will play a pivotal role toward this transition,[2] in which fuel cells will be a main component. For their operation, sustainable supply of large volumes of hydrogen is a requisite. The most environmentally sustainable method of obtaining hydrogen is through water splitting, where hydrogen is produced in the cathode of an electrolyzer through the hydrogen evolution reaction (HER),[3] while oxygen is produced in the anode through oxygen evolution reaction (OER). Due to sluggish reaction kinetics, requiring a high amount of energy, electrocatalysts are used to overcome the reaction activation barrier and accelerate both HER and OER. Pt and other noble metals are currently the most efficient electrocatalysts, but their high cost and scarcity impede their widespread application.[4–6] The quest of alternative electrocatalysts that can efficiently replace noble metals is a major challenge.

Transition metal (TM)-based composites hold great promise in replacing noble metals for HER, thanks to their intrinsic electrocatalytic efficiency and good chemical stability in harsh acidic conditions.[7] Particular attention has been given to TM carbides

S. Chaitoglou, Y. Ma, R. Amade-Rovira, E. Bertran-Serra
Department of Applied Physics
University of Barcelona
C/Martí i Franques, 1, 08028 Barcelona, Catalunya, Spain
E-mail: stefanoschaitoglou@ub.edu

S. Chaitoglou, Y. Ma, R. Amade-Rovira, E. Bertran-Serra
ENPHOCAMAT Group
Institute of Nanoscience and Nanotechnology (IN2UB)
University of Barcelona
C/ Martí i Franques, 1, 08028 Barcelona, Catalunya, Spain

The ORCID identification number(s) for the author(s) of this article can be found under https://doi.org/10.1002/aesr.202500016.

© 2025 The Author(s). Advanced Energy and Sustainability Research published by Wiley-VCH GmbH. This is an open access article under the terms of the Creative Commons Attribution License, which permits use, distribution and reproduction in any medium, provided the original work is properly cited.

DOI: 10.1002/aesr.202500016

S. Ghosh, C. S. Casari
Department of Energy
Micro and Nanostructured Materials Laboratory — NanoLab
Politecnico di Milano
via Ponzio 34/3, 20133 Milano, Italy
E-mail: subrata.ghosh@pw.edu.pl

S. Ghosh
Faculty of Mechatronics
Warsaw University of Technology
św. A. Boboli 8, 02-525 Warsaw, Poland

R. Ospina
Escuela de Física
Universidad Industrial de Santander
Carrera 27 Calle 9 Ciudad Universitaria, Bucaramanga 681011, Colombia

26999412, 0, Downloaded from https://advanced.onlinelibrary.wiley.com/doi/10.1002/aesr.202500016 by CochraneItalia, Wiley Online Library on [25/08/2025]. See the Terms and Conditions (https://onlinelibrary.wiley.com/terms-and-conditions) on Wiley Online Library for rules of use; OA articles are governed by the applicable Creative Commons License

(TMCs), especially Mo_2C and WC, whose efficiency is foreseen to match noble metals. These materials are stable in high working temperatures, abundant, and relatively cheap, compared to noble metals. The enhanced electrocatalytic performance of TMCs, compared to parent TMs, originates from the incorporation of carbon in interstitial sites of the TM. This results in an increased metal–metal bond distance which leads to a contraction of the metal d-band and a higher density of states near the Fermi level, resulting in a better overall electrocatalytic performance.[8] The preparation of nanocomposites based on the above materials (carbons and TMCs) is one of the most promising implemented strategies to fabricate electrodes with an enhanced number of electrocatalytically active sites. Examples include the synthesis of TMC in the form of nanoparticles[9] and nanowires.[10] In addition to the above, the use of nanostructured support materials has been proven to be beneficial in providing a high surface-to-volume ratio, enabling the dispersion of large amounts of catalytic materials in their matrix.[11] For this purpose, carbon-based porous materials are considered one of the ideal platforms. Carbon composites can form a plethora of nanostructures, for example, graphene[12] and graphene derivatives, like graphene nanowalls[13] and laser-induced graphene,[14] carbon foam,[15] and carbon nanotubes.[16] They stand out thanks to their remarkable chemical stability in harsh conditions and high electron conductivity.[17] Nevertheless, moderate porosity and preferential growth orientations characterize in many cases the above nanostructures, which makes the homogeneous dispersion of active material challenging. This is especially the case in composite materials requiring two or multistep processes, in which the support material is prepared first, followed by the deposition of the active material. For example, deposition of thin films via sputtering and/or evaporation can be inefficient due to shadowing effects,[7,18] meanwhile deposition of nanoparticles via wet chemistry approaches can result in the formation of agglomerations, limiting their catalytic efficiency.[19] The deposition of nanostructured support and catalytic material in a single step has risen as an approach to overcome the above critical issue. Recently, the capacity to deposit metallic particles in carbon foams through a one-step pulsed laser deposition (PLD) process,[20,21] as well as multistep PLD process, is demonstrated.[22,23] The process involved a single-step PLD production run using two different-size targets (metal nitride target and graphite target) placing one onto another and ablating simultaneously with a single-laser beam, resulting in the preparation of carbon/titanium oxynitride and carbon/vanadium oxynitride nanofoams as energy storage electrodes.[20]

In the present work, we extend the above studies by probing the deposition of carbon/W and carbon/WC composites. We demonstrate the capacity to precise control the ratio of elemental constituents by manipulating the laser ablation spot position. In addition, postdeposition high-temperature annealing step is applied, to carburize and crystallize the W nanoparticles, adding two features that are known to improve the catalytic performance of TMs.[24] The nanocomposites are employed as cathodic electrodes, to study their efficiency to catalyze hydrogen evolution in an acidic medium. While the deposition of tungsten carbide via laser ablation has been reported before,[25] this study provides novel insights on the preparation of advanced composites, with an emphasis on the synthesis of composites featuring a controlled and homogeneous dispersion of metallic nanoparticles embedded in a porous and conductive carbon matrix. Remarkably, the strategy of simultaneous ablation of two targets, a metal and graphite, can be applied to the wider family of metals that can be ablated, unlocking further opportunities for application in electrochemical and other desired applications.

2. Experimental Section

Synthesis: Carbon nanofoam composite was synthesized by PLD at room temperature placing 1-inch graphite target onto tungsten-based targets (tungsten (W) and tungsten carbide (WC)). All targets were purchased from Testbourne B. V. and the purity was 99.99%. The nanosecond PLD setup used the second harmonic ($\lambda = 532$ nm) of a Q-switched Nd:YAG laser (pulse duration of 5–7 ns), with a repetition rate of 10 Hz and a fluence of 11 J cm^{-2}. Laser spot size on single target was estimated in ambient environment to be 0.056 cm^2. The simultaneous ablation from both targets was carried out at two different positions, as indicated in **Scheme 1**. The target was placed on a rotating/translating holder to ablate the target uniformly, while the Si (100) and carbon paper substrates were placed on the rotating substrate holder to deposit the nanostructure homogeneously over the desired area. The distance between the top target (graphite) and substrate of 40 mm was maintained during deposition. Prior to deposition, the chamber was evacuated down to the base pressure of 2×10^{-3} Pa using first a rotary pump followed by a turbomolecular pump. The deposition was carried out with two steps: ablation for 2 min at the pressure of 10^{-2} Pa to grow a compact film as an adhesive layer between substrate and porous film followed by 10 min deposition under 99% Ar gas at 500 Pa to grow the highly porous nanofoam composite. After the synthesis, thereafter, the deposition unit was vented by allowing air inside the chamber upon competition of synthesis process and the as-deposited nanostructures were taken out for further studies. The deposition was carried out on Si (100) and carbon paper (Toray 090, purchased from Fuell Cell store) substrate. The deposition on Si was used for standard characterizations while the nanofoam composite on carbon paper was used for the electrocatalytic hydrogen evaluation measurement.

Postdeposition thermal annealing of the pristine samples was performed in a quartz oven. After inserting the sample, the oven was heated to 950 °C. Annealing duration was 30 min. After annealing, the over was cooled to room temperature, before removing the sample. Ar was introduced in the oven with a stable flow of 20 sccm during heating, annealing, and cooling steps. The pressure was kept stable at 1 Pa with the assistance of a rotary valve.

Structural and chemical characterization: The sample structure and morphology were examined using scanning electron microscopy (SEM) and transmission electron microscopy (TEM). Energy-dispersive X-ray spectroscopy (EDS) was employed to determine the elemental composition of the samples. X-ray photoelectron spectroscopy (XPS) and X-ray diffraction (XRD) measurements were employed to study the chemical state and crystal structure. Raman spectroscopy was employed to study the vibrational modes. Detailed description

© 2025 The Author(s). Advanced Energy and Sustainability Research published by Wiley-VCH GmbH

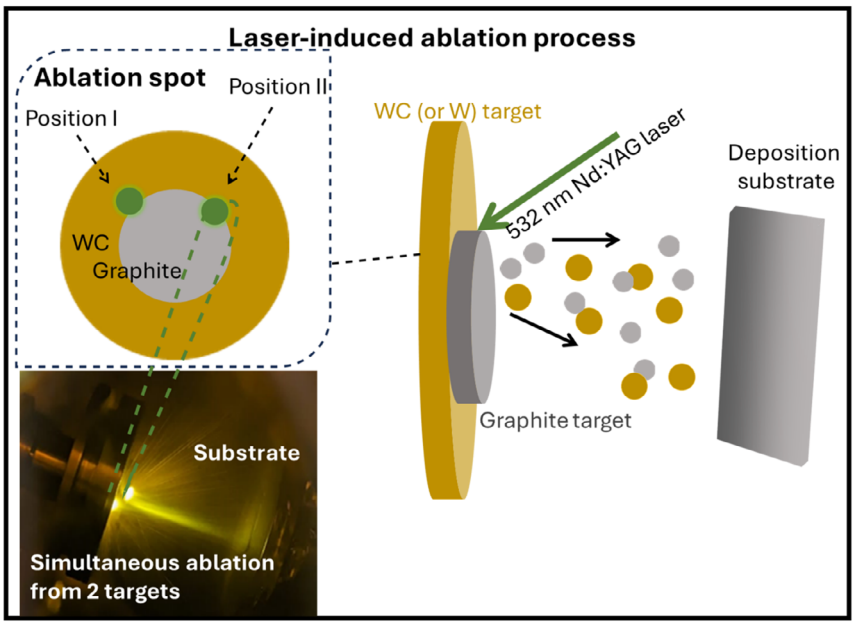

Scheme 1. Illustration of two-target assembly and simultaneous ablation from two distinct spots (visible as distinct spots in optical micrograph) irradiated during the laser-induced ablation deposition.

of the instrumentation and measurement conditions is reported in previous works.[26]

Electrochemical characterization: The electrochemical behavior of the sample for the HER was analyzed using a potentiostat/galvanostat (AutoLab, PGSTAT30, Eco Chemie B.V.). A three-electrode system was employed at room temperature for the experiments. An Ag/AgCl electrode with an internal 3 M KCl solution functioned as the reference electrode, while a graphite felt (Metrohm) served as the counter electrode. The samples acted as the working electrode, connected to the power source via a crocodile clip, and were cut to provide a surface area of 1 cm^2. Linear sweep voltammetry was conducted at a scan rate of 5 $mV\,s^{-1}$ using a 0.5 M H_2SO_4 electrolyte. Chronoamperometry was performed to evaluate electrode stability, applying a constant bias of 290 mV versus reverse hydrogen electrode (RHE). Electrochemical impedance spectroscopy (EIS) was used to determine the charge transfer resistance, with measurements taken over a frequency range of 100 kHz–0.1 Hz. Cyclic voltammetry (CV) scans were carried out to calculate the double-layer capacitance and electrochemically active surface area. All potentials were converted to the RHE scale using the Nernst equation $E_{RHE} = E_{Ag/AgCl} + 0.21 + 0.050x$ pH.

3. Results and Discussion

A schematic illustration of the preparation process is depicted in Scheme 1. The carbon paper consists of a dense network of carbon fibers, macroscopically assembling a paper-like structure (**Figure 1**a and digital photograph in inset). The morphology of the as-deposited W (or WC)/ carbon composite on carbon paper is shown in Figure 1b. It features a porous structure with a nanofoam-like morphology (high-magnification SEM image in Figure S1, Supporting Information). EDS elemental mapping analysis shows the homogeneous distribution of W on the carbon support (Figure 1c). A side view image of the composite was taken for a sample deposited under the same conditions on a Si substrate (Figure 1d). The height of the composite is ≈3 µm. The homogeneous deposition of W (and adsorption of O) across the vertical axe of the carbon composite is further confirmed by the EDS elemental mapping analysis (Figure 1e). EDS analysis shows that the W/C weight ratio can be controlled by manipulating the laser ablation position on the graphite/ W (or WC) target interface (see schematic and results in Figure 1f, bottom).[20]

Even though these results cannot provide the precise stoichiometry of the composite (since the C signal originates from both the nanocomposite and the support substrate), they serve as a guide to confirm the capacity to tune W deposition. Therefore, for each TM-based target, two distinct samples were prepared, one in which the ablation occurs on a spot in the center of the graphite–W (or WC) interface (position II in Scheme 1) and one in which the ablation occurs on a spot centered slightly on the tungsten side of the graphite–W (or WC) interface (position I in Scheme 1). When ablation occurs in position I, it results in enhanced W wt% values, compared to those for ablation occurring in position II (**Table 1**). The pure deposition of W and C on the support substrate is confirmed by the EDS spectrum, which shows no traces of other elements (Figure 1f, top).

The Raman fingerprints of the pristine and annealed WC/ carbon nanofoam composite (with high W content) are depicted in **Figure 2**a. The pristine (as-deposited) composite exhibits major peaks centered at 263, 695, and 803 cm^{-1}, which are typically attributed to WC and WC-O.[27,28] Additionally, peaks originating from the carbon composite are centered at 1371 (defect-activated D peak of graphitic carbon) and 1597 cm^{-1}

© 2025 The Author(s). Advanced Energy and Sustainability Research published by Wiley-VCH GmbH

26999412, 0, Downloaded from https://advanced.onlinelibrary.wiley.com/doi/10.1002/aesr.202500016 by CochraneItalia, Wiley Online Library on [25/08/2025]. See the Terms and Conditions (https://onlinelibrary.wiley.com/terms-and-conditions) on Wiley Online Library for rules of use; OA articles are governed by the applicable Creative Commons License

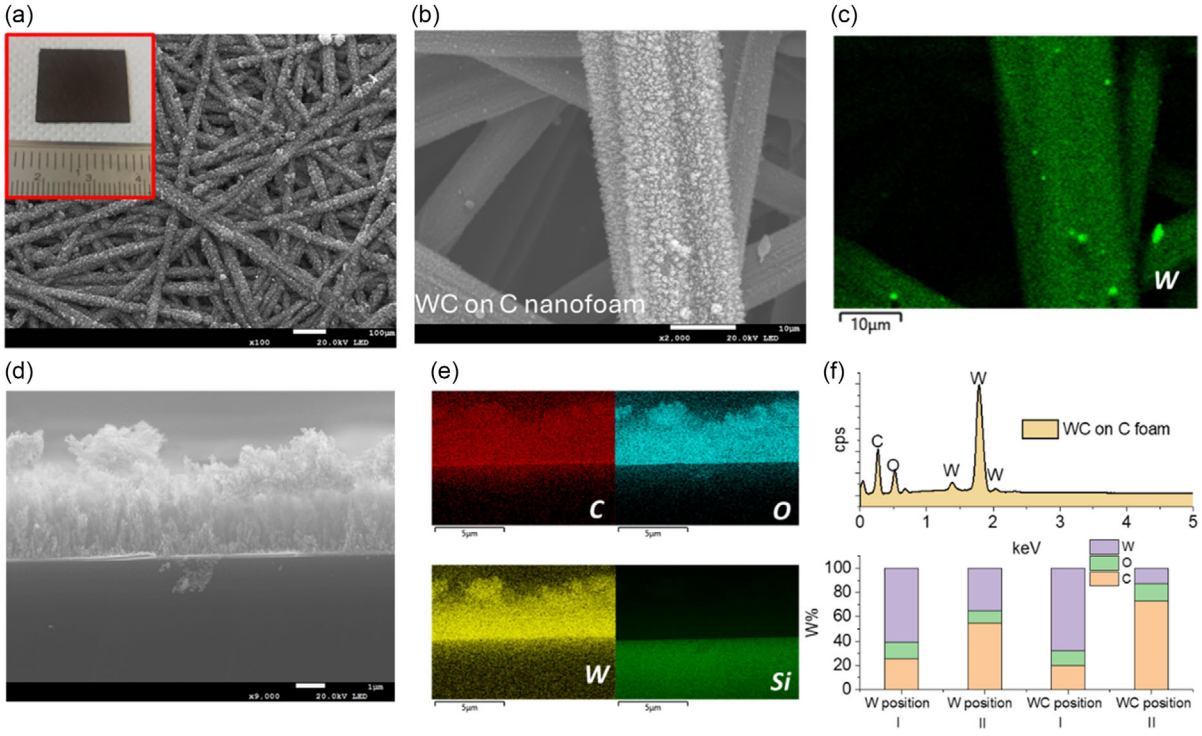

Figure 1. Morphological characterization of the deposited composites. a) SEM image of the WC/carbon nanofoam composite on carbon paper and digital photograph of the sample (inset), b) SEM image of the nanocomposite in higher magnification, c) EDS mapping of W, showcasing the homogeneous distribution, d) SEM image of the WC/carbon nanofoam deposited on a Si substrate, e) EDS mapping of W, C, O and Si, to showcase the homogeneous distribution of W, C, and O, and f) EDS spectra of the resulting nanocomposite (top) and elemental wt% distribution as a function of used target and selected ablation spot.

Table 1. Weight % results of carbon, oxygen, and tungsten, as derived from EDS spectra analysis.

Sample	C [wt%]	O [wt%]	W [wt%]
W/Carbon nanofoam composite-1 (high W load)	25	14	61
W/Carbon nanofoam composite-2 (low W load)	55	10	35
WC/Carbon nanofoam composite-1 (high W load)	20	12	68
WC/Carbon nanofoam composite-2 (low W load)	73	14	13

(G peak of graphite, due to in-plane carbon–carbon stretching mode). The high intensity of the D band and the width and shape of the G band reveal that the as-deposited carbon composite is relatively amorphous and contains a high density of structural defects[29] (black graph). After annealing, the intensity of the W composite-associated peaks increases, due to the formation of larger W particles via sintering.[30] The G peak of graphite is sharper and well separated from the D peak, indicating graphitization of the carbon structure. This is additionally confirmed by the rise of the 2D peak at 2707 cm^{-1} (blue graph). XRD characterization reveals the crystal fingerprint of the pristine and annealed composites (Figure 2b). Sherrer equation is applied to quantify the crystallite size of the carbon support, based on the (002) diffraction peak. A crystallite size of ≈2.2 nm is calculated, which confirms Raman spectroscopy regarding the amorphous-like nature of the carbon nanofoam.[31] Upon annealing, diffraction peaks originating from the carbide phases rise (JCPDS 00-035-0776 and 00-051-0939, noted with either asterisk or diaeresis in the blue graph). Moreover, the main diffraction peak of the oxide phase at 36.8°, initially present in the pristine sample (JCPDS 00-032-1393, black graph), diminishes upon the annealing step, proving the efficient carburization and crystallization of the initially severely oxidized WC/carbon nanofoam composite.[32–34] In conclusion. the resulting hybrid composite is not a pure carbide but a hybrid structure consisting of both carbide and oxide domains.

TEM characterization of the pristine and annealed composites provides insights into their synthesis and evolution upon thermal annealing. A high-resolution image of the as-deposited nanoparticles shows that they are predominantly single crystals of both tungsten carbide (evidenced by the (101) of WC) and oxide (evidenced by the (210) of WO_2) (**Figure 3**a). A lower-magnification image shows the homogeneous distribution and separation of the nanoparticles supported on the carbon film (Figure 3b). They exhibit a very narrow size distribution, with all particles having a diameter of approximately ≈3–4 nm (see histogram in Figure 3c). Upon high-temperature thermal annealing, nanoparticles coalesce to form polycrystalline domains (Figure 3d). The sintering of metallic nanoparticles during high-temperature thermal annealing is a well-known phenomenon that can alter their properties.[35] These domains consist of both oxide and carbide tungsten crystals. Furthermore, a thin carbon shell of ≈2–3 nm

© 2025 The Author(s). Advanced Energy and Sustainability Research published by Wiley-VCH GmbH

26999412, 0, Downloaded from https://advanced.onlinelibrary.wiley.com/doi/10.1002/aesr.202500016 by CochraneItalia, Wiley Online Library on [25/08/2025]. See the Terms and Conditions (https://onlinelibrary.wiley.com/terms-and-conditions) on Wiley Online Library for rules of use; OA articles are governed by the applicable Creative Commons License

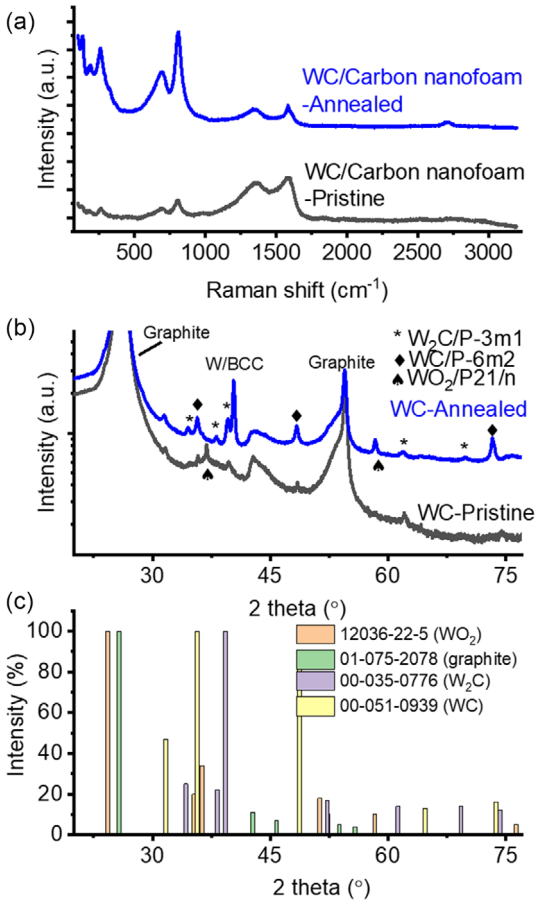

Figure 2. a) Raman spectra of the as-deposited (black graph) and annealed nanocomposite (blue graph), b) XRD spectra of the as-deposited (black graph) and annealed nanocomposite (blue graph), and c) standard diffraction cards.

thick is observed on the surface of the nanoparticles (marked with a red arrow in Figure 3d). Such shells are commonly formed when carbide materials are synthesized through heat treatment with carbon-containing gas precursors, as the carbon foam and can significantly enhance the stability of the nanoparticles. It has been suggested that the shell may inhibit oxidation of the nanoparticle by acting as a mechanical barrier, thereby preventing volume expansion associated with oxidation.[36] This could explain why the WC composite retains its strong catalytic activity over an extended period, as it will be shown in the electrochemical characterization section. However, it is worth noting that the carbon shell does not serve as a complete chemical barrier, as molecules can still penetrate it and access the catalytically active sites on the surface of the WC. The resulting composites upon annealing are predominantly carbide phases, as revealed by the XRD data shown above, suggesting removal and evaporation of oxygen. Nanoparticles form large agglomerations of hundreds of nanometers (Figure 3e). The individual domains have a broad distribution of diameters, between ≈40 and 100 nm (with an average diameter value of 65.1 ± 13.7 nm, Figure 3f).

The surface states of the pristine and annealed WC/carbon nanofoam composites were characterized by XPS (**Figure 4**). Figure 4a shows the C 1s peak of pristine WC. Deconvolution of the spectrum reveals components related to C—OOH, C═OH, C—C, and C—W, centered at 288.6, 286.3, 284.6, and 282. 8 eV, respectively. Upon annealing, a C—O component rises at 285.6 eV and the C—W component is enhanced, as evidenced by the right-shoulder rise in the envelope spectrum (Figure 4d). Deconvolution of the O 1s peak of the pristine sample shows the presence of components assigned to O—COH and O—W, centered at 531.7 and 530.8 eV, respectively. The annealed composite exhibits an increase of O—COH signal and a decrease of the O—W signal (Figure 4b,e). Thus, during the annealing step, W is reduced and oxygen reacts with the carbon foam support. Deconvolution of the W 4f peak of the pristine sample shows peaks assigned to WO_3 and WO_2, centered at 38 and 35.8 eV (for WO_3) and 34.7 and 32.5 eV (for WO_2). Weak satellite peaks attributed to metallic and carburized W are also apparent (Figure 4c).[37,38] In the annealed composite, the signal originating from carburized W is enhanced, as evidenced by the rise of the components centered at 33.9 and 31.8 eV (Figure 4f). The XPS analysis confirms the carburization of the initially oxidized surface of the W nanoparticles upon the high-temperature annealing step.

The electrocatalytic efficiency of the composites toward HER is evaluated via linear sweep voltammetry (LSVs), CVs, and EIS characterization. The as-deposited WC/carbon nanofoam composite-1 (with high W load) exhibits the lowest overpotential value of -349 mV, required for the generation of 10 mA cm^{-2}. Respectively, the as-deposited WC/carbon nanofoam composite-2 (with low W load) requires -568 mV for the generation of 10 mA cm^{-2}. The as-deposited W/carbon nanofoam composite-1 (with high W load) exhibits an overpotential value of –350 mV, required for the generation of 10 mA cm^{-2} and the as-deposited W/carbon nanofoam composite-2 (with low W load) requires –560 mV. The pristine carbon foam does not show any electrocatalytic activity in the examined voltage window (LSV graphs, **Figure 5**a). From these results, it becomes evident that the composites with high W load (for both the pristine W and WC targets) show enhanced activity, compared to those with low W load. The two highly loaded composites (WC/carbon nanofoam composite-1 and W/carbon nanofoam composite-1) require the same overpotential to generate 10 mA cm^{-2}. Nevertheless, for higher current densities, the as-deposited carbide composite requires lower overpotentials (e.g., –487 mV the W/carbon nanofoam composite-1 and –540 mV the W/carbon nanofoam composite-1, for the generation of 100 mA cm^{-2}). CV measurements on the high and low load composites are carried out at varying scan rates, from 10 to 200 mV s^{-1} (Figure 5 left and right). The linear fitting of the current density with respect to scan rate is used to calculate the capacitance of each composite, according to

$$I = \frac{dQ}{dt} = \frac{dQ}{dV} \times r_{sc} = C \times r_{cs} \quad (1)$$

where r_{sc} is the scan rate and C the capacitance (Figure 5c). Therefore, the high W load composite exhibits a capacitance of ≈5 mF cm^{-2}, while the low W load composite exhibits a capacitance of ≈0.5 mF cm^{-2}. This tenfold increase in capacitance further supports the correlation between higher W loading and

© 2025 The Author(s). Advanced Energy and Sustainability Research published by Wiley-VCH GmbH

26999412, 0, Downloaded from https://advanced.onlinelibrary.wiley.com/doi/10.1002/aesr.202500016 by CochraneItalia, Wiley Online Library on [25/08/2025]. See the Terms and Conditions (https://onlinelibrary.wiley.com/terms-and-conditions) on Wiley Online Library for rules of use; OA articles are governed by the applicable Creative Commons License

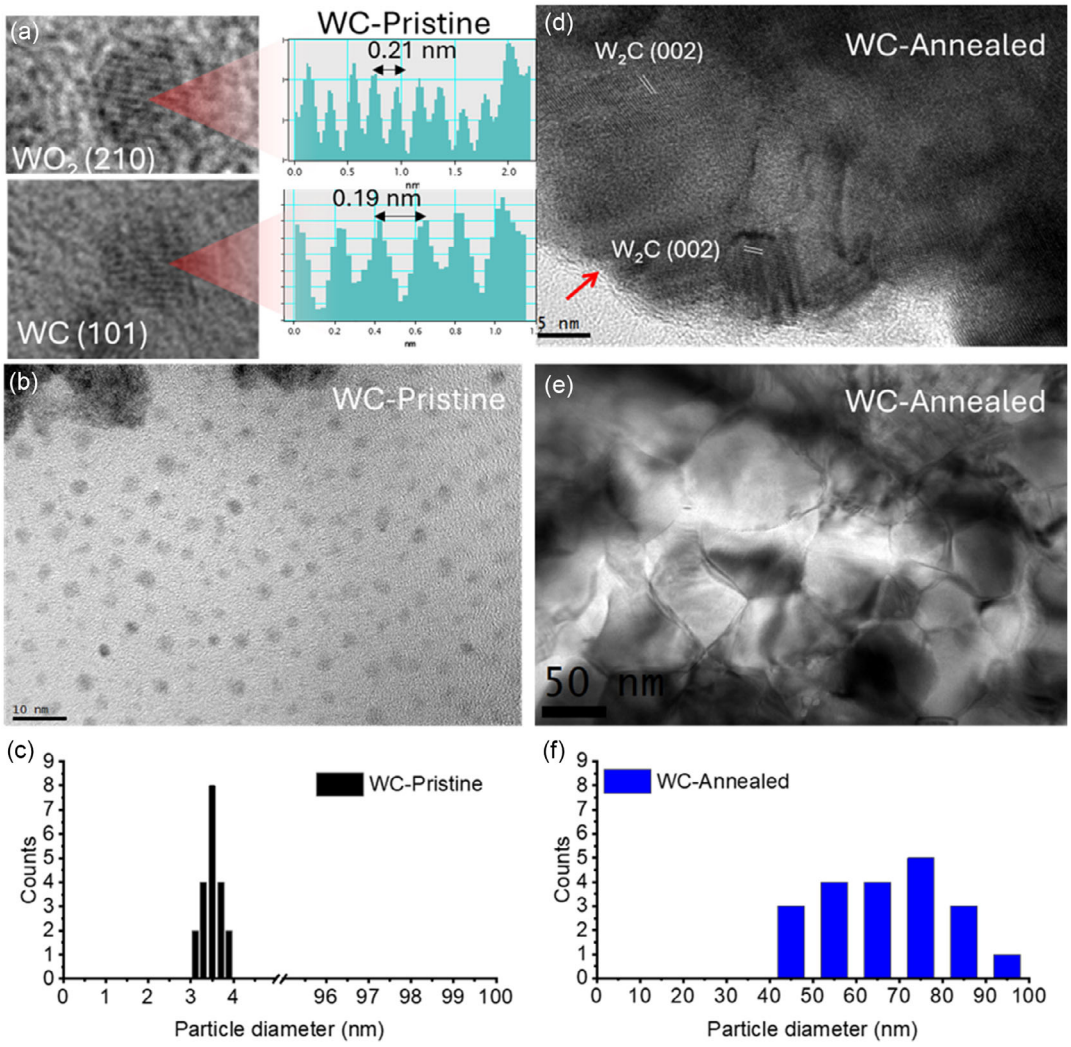

Figure 3. Morphological characterization. TEM images of the as-deposited (pristine) nanocomposite in high resolution (a, scale bar 5 nm) and lower magnification (b, scale bar 10 nm). c) Diameter distribution histogram of the pristine nanoparticles. TEM images of the annealed nanocomposite in high resolution (scale bar 5 nm) d) and lower magnification (e, scale bar 50 nm). f) Diameter distribution histogram of the annealed nanoparticles.

enhanced electrocatalytic performance, as outlined earlier. The ≈200 mV difference in required overpotentials between the high-load and low-load composites is attributed to the presence of more electrocatalytically active sites in the firsts.[39] In addition, the slightly enhanced activity, especially in higher current densities, of the carbide composite, confirms the positive impact of carbon species in accelerating reaction kinetics.[8] The LSV curves of the annealed composites are exhibited in Figure 5d. The same trend as with the pristine samples is observed; the high-W load composites exhibit enhanced activity toward HER. Between the two, the carbide composite has a slightly enhanced activity compared to the pure TM composite. Overall, the activity of the annealed composites is improved. In detail, the annealed WC/carbon nanofoam composite-1 (with high-W load) exhibits the lowest overpotential value of –276 mV, required for the generation of 10 mA cm^{-2}. Respectively, the annealed WC/carbon nanofoam composite-2 (with low-W load) requires –325 mV for the generation of 10 mA cm^{-2}. The annealed W/carbon nanofoam composite-1 (with high-W load) exhibits an overpotential value of –287 mV, required for the generation of 10 mA cm^{-2} and the annealed W/carbon nanofoam composite-2 (with low-W load) requires –519 mV, respectively. The enhanced HER activity of the annealed composites is attributed to higher conductivity and more ordered atomic arrangement, induced by the crystallization and carburization of the sample.[40] The initially pristine W-based composites are carburized during the annealing step, as confirmed by XRD characterization via the rise of peaks (absent to the as-deposited sample) attributed to W_2C (Figure S2, Supporting Information). Figure 5e shows the Tafel slopes of all composites. The low W load composites (W/carbon nanofoam composite-2 and WC/carbon nanofoam composite-2) show the larger Tafel slope values of 146 and 101 mV dec^{-1}, respectively. The high-W load composites (W/carbon nanofoam composite-1 and WC/carbon

© 2025 The Author(s). Advanced Energy and Sustainability Research published by Wiley-VCH GmbH

26999412, 0, Downloaded from https://advanced.onlinelibrary.wiley.com/doi/10.1002/aesr.202500016 by CochraneItalia, Wiley Online Library on [25/08/2025]. See the Terms and Conditions (https://onlinelibrary.wiley.com/terms-and-conditions) on Wiley Online Library for rules of use; OA articles are governed by the applicable Creative Commons License

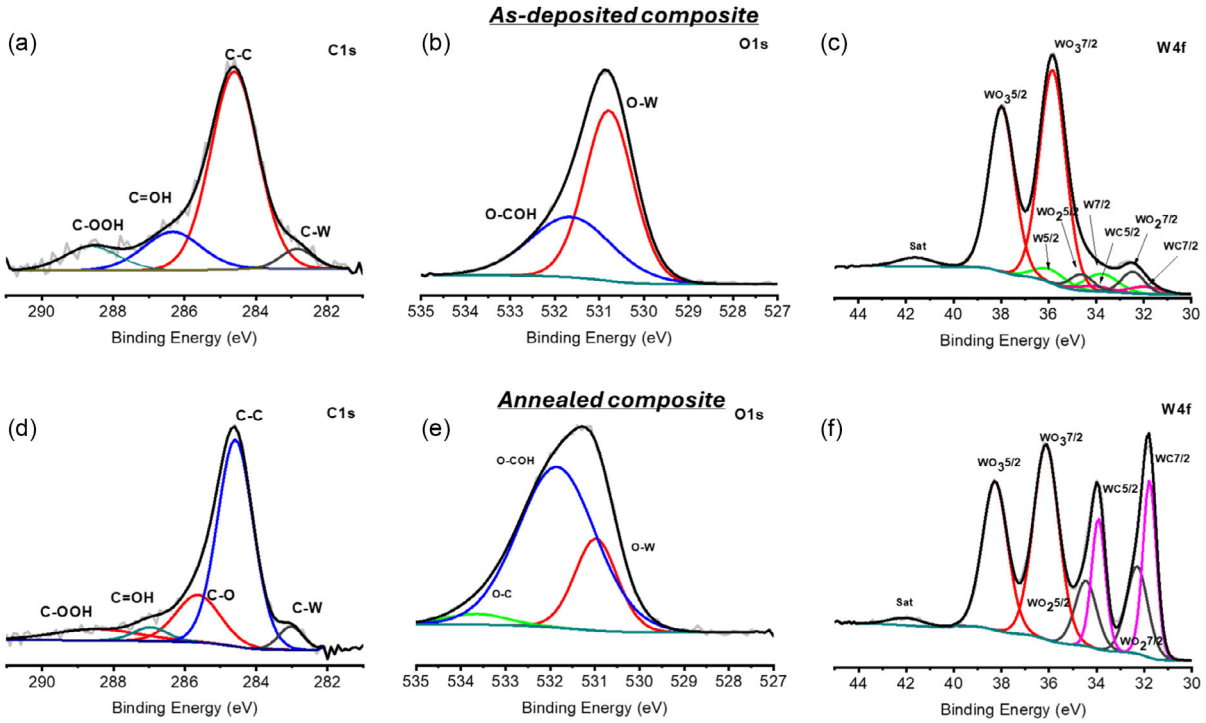

Figure 4. XPS spectra of as-deposited WC/carbon nanofoam: a) C 1s spectrum, b) O 1s spectrum, and c) W 4f spectrum. XPS spectra of annealed WC/carbon nanofoam: d) C 1s spectrum, e) O 1s spectrum, and f) W 4f spectrum.

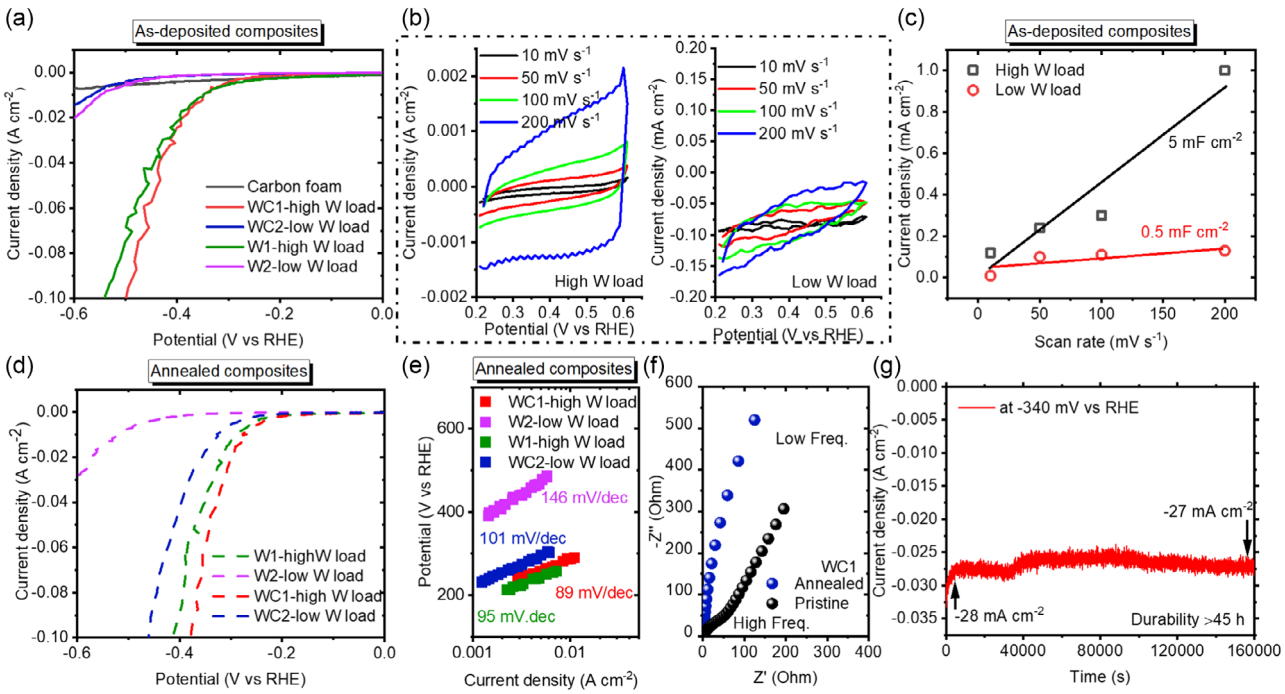

Figure 5. a) LSV curves of as-deposited W and WC composites. b) CV scans of as-deposited WC composite with a high (left) and low (right) W load. c) Plot of current density with respect to scan rates applied during CV, for as-deposited WC composite with a high and low W load. d) LSV curves of annealed W and WC composites. e) Tafel slopes of annealed W and WC composites. f) EIS curves of the WC1 composite in pristine and annealed state. g) Chronoamperometry test during 45 > h under −340 mV continuous bias.

© 2025 The Author(s). Advanced Energy and Sustainability Research published by Wiley-VCH GmbH

26999412, 0, Downloaded from https://advanced.onlinelibrary.wiley.com/doi/10.1002/aesr.202500016 by CochraneItalia, Wiley Online Library on [25/08/2025]. See the Terms and Conditions (https://onlinelibrary.wiley.com/terms-and-conditions) on Wiley Online Library for rules of use; OA articles are governed by the applicable Creative Commons License

nanofoam composite-1) show the smaller Tafel slope values of 95 and 89 mV dec^{-1}, respectively, which confirm the faster reaction kinetics rates. These results suggest that HER over the high-W load nanostructures follows the Volmer–Heyrovsky mechanism with the rate-determining step shifting from Volmer (primary discharge) reaction to Heyrovsky (electrochemical desorption) reaction.[41] EIS is utilized to gain insights into the conductivity of as-deposited and annealed samples (Figure 5f). The annealed sample (black dots) demonstrates a steeper slope at low frequencies, indicating rapid charge transport kinetics.[42,43] The durability of the most efficient composite (annealed WC/carbon nanofoam composite-1 with high- W load) is tested by chronoamperometry measurement at a constant overpotential of -340 mV. The current density remains remarkably stable over 45 h of operation, exhibiting only a small decrease in its value, from –28 to –27 mA cm^{-2} (Figure 5g). Additional chronoamperometry tests were carried out in higher applied potential, to demonstrate the stability of the composite in high current densities. Stable performance was recorded for 1 h of operation for current densities of −35, −75, and −580 mA cm^{-2}, respectively (Figure S3, Supporting Information), which are especially significant for water electrolysis under high rates.[44] These findings highlight the promising potential of hybridizing W-based composites with carbon-based materials for use in electrocatalytic hydrogen evolution applications.[26,45–47]

Characterization of the composite after the chronoamperometry test was performed to evaluate its structural and chemical stability. SEM imaging reveals that the composite retains its key morphological features, including the foam-like structure with high porosity, even after the test. EDS analysis indicates the presence of residual sulfur (S), likely from the electrolyte used during the experiment, which has been deposited onto the surface of the composite (Figure S4a,b, Supporting Information). To further assess the surface chemistry, XPS measurements were conducted. The W4f peaks in the XPS spectrum show that the surface of the composite underwent complete oxidation following the chronoamperometry test. The characteristic peaks for metallic and carburized tungsten are no longer detectable, with only the $W4f_{5/2}$ and $W4f_{7/2}$ peaks corresponding to WO_3 remaining visible (Figure S4c, Supporting Information). XRD analysis also confirms these findings, revealing peaks attributed to both W carbide and W oxide phases at 34.3°, 38°, and 35.5°, respectively (Figure S4d, Supporting Information). Based on this comprehensive characterization, it can be concluded that oxidation primarily occurs at the surface of the composite, while the underlying carbide phases remain largely intact and electrocatalytically active. This explains the composite's endurance during the chronoamperometry test, as the core material retains its catalytic properties despite the surface oxidation.

4. Conclusion

In summary, this work demonstrates the effectiveness of simultaneous laser ablation of two targets—TM and graphite—as a robust method for synthesizing 3D porous carbon/TM carbide composites. By adjusting the laser ablation position, the stoichiometry of the resulting composite can be precisely controlled. Morphological characterization confirms the homogeneous embedding of the TM within the carbon foam, forming a highly dense network of nanoparticles. The annealing process promotes carburization and crystallization, enhancing the electrocatalytic performance of the composites for hydrogen evolution. The optimized nanostructures show efficient electrocatalytic activity, with low overpotentials (e.g., −278 mV at 10 mA cm^{-2}) and exceptional stability during long-term operation (up to 45 h under a constant applied potential and maintaining high current densities up to 580 mA cm^{-2}). The enhanced catalytic activity of the composite is attributed to the 1) enhanced activity of TMCs, compared to parent TMs; 2) the presence of more electrocatalytically active sites on the composite with high W load, resulting in more efficient hydrogen evolution; And 3) use of a conductive support structure (carbon nanofoam) which provides an enhanced surface area for anchoring metallic particles and permits the assembly of binder-free electrodes. These results highlight the ability to create highly homogeneous carbon-supported metallic composites, which hold significant potential for applications in the energy sector and other advanced technological fields.

Supporting Information

Supporting Information is available from the Wiley Online Library or from the author.

Acknowledgements

The authors acknowledge financial support from grants TED2021-132070B-C21 and PDC2021-121868-C22, funded by MCIN/AEI/10.13039/501100011033 and by the "European Union" or by the European Union NextGenerationEU/PRTR and from grant project no. 2021SGR00936, funded by AGAUR of Generalitat de Catalunya. The authors would like to thank the CCiT (Scientific and Technological Center)-UB for access to the structural and morphological characterization facilities. S.C. acknowledges support from the MSCA fellowship funded by the European Commission through grant agreement 101062014 (HORIZON Europe-MSCA-2021-PF-01). S.G. acknowledges Horizon Europe (HORIZON) for the Marie Sklodowska-Curie Fellowship (grant no. 101067998-ENHANCER). C.S.C. acknowledges funding by the project under the National Recovery and Resilience Plan (NRRP), Mission 4 Component 2 Investment 1.3 - Call for tender no. 341 of 15.03.2022 of Ministero dell'Università e della Ricerca (MUR), funded by the European Union – NextGenerationEU Award number: project code PE0000021, Concession Decree no. 1561 of 11.10.2022 adopted by Ministero dell'Università e della Ricerca (MUR), CUP D43C22003090001, Project title "Network 4 Energy Sustainable Transition_NEST."

Conflict of Interest

The authors declare no conflict of interest.

Author Contributions

Stefanos Chaitoglou: conceptualization (equal); data curation (lead); investigation (lead); methodology (lead); resources (supporting); writing—original draft (lead). **Subrata Ghosh**: conceptualization (lead); investigation (equal); methodology (lead); writing—original draft (equal). **Rogelio Ospina**: data curation (equal); formal analysis (equal); writing—original draft (supporting). **Yang Ma**: Data curation (equal); Formal analysis (equal). **Roger Amade-Rovira**: formal analysis (equal); project administration (lead); supervision (equal); writing—original draft (equal).

© 2025 The Author(s). Advanced Energy and Sustainability Research published by Wiley-VCH GmbH

26999412, 0, Downloaded from https://advanced.onlinelibrary.wiley.com/doi/10.1002/aesr.202500016 by CochraneItalia, Wiley Online Library on [25/08/2025]. See the Terms and Conditions (https://onlinelibrary.wiley.com/terms-and-conditions) on Wiley Online Library for rules of use; OA articles are governed by the applicable Creative Commons License

Carlo S. Casari: methodology (equal); supervision (equal); writing—original draft (equal). **Enric Bertran-Serra**: methodology (equal); supervision (equal); writing—original draft (supporting).

Data Availability Statement

The data that support the findings of this study are available from the corresponding author upon reasonable request.

Keywords

carbon composites, hydrogen evolution reactions, pulsed laser deposition, transition metal composites

Received: January 13, 2025
Revised: February 7, 2025
Published online:

[1] A. Toktarova, L. Göransson, F. Johnsson, *Int. J. Hydrogen Energy* **2024**, https://doi.org/10.1016/j.ijhydene.2024.08.016.
[2] M. Gidden, T. Gasser, G. Grassi, N. Forsell, I. Janssens, W. Lamb, J. Minx, Z. Nicholls, J. Steinhauser, K. Riahi, *Nature* **2023**, *624*, 102.
[3] F. Yu, L. Yu, I. Mishra, Y. Yu, Z. Ren, H. Zhou, *Mater. Today Phys.* **2018**, *7*, 121.
[4] H. D. Mai, S. Jeong, G. Bae, N. M. Tran, J. Youn, C. Park, K. Jeon, *Adv. Energy Mater* **2023**, *13*, 2370097.
[5] W. Cai, X. Liu, L. Wang, B. Wang, *Mater. Today Nano* **2022**, *17*, 100144.
[6] Y. Saira, Z. Li, Y. Zhu, Q. Liu, W. Luo, Y. Wang, M. Gong, G. Fu, Y. Tang, *Chem. Commun.* **2024**, *60*, 2768.
[7] Y. Zhang, B. Zhang, Z. Yin, X. Ma, Y. Zhou, *New J. Chem.* **2022**, *46*, 11893.
[8] J. G. Chen, *Chem. Rev.* **1996**, *96*, 1477.
[9] Y. Huang, Q. Gong, X. Song, K. Feng, K. Nie, F. Zhao, Y. Wang, M. Zeng, J. Zhong, Y. Li, *ACS Nano* **2016**, *10*, 11337.
[10] H. Lin, Z. Shi, S. He, X. Yu, S. Wang, Q. Gao, Y. Tang, *Chem. Sci.* **2016**, *7*, 3399.
[11] M. Smiljanić, B. Grgur, *Front. Chem.* **2024**, *12*, 1373189.
[12] S. Chaitoglou, T. Giannakopoulou, G. Papanastasiou, D. Tsoutsou, A. Vavouliotis, C. Trapalis, A. Dimoulas, *Appl. Surf. Sci.* **2020**, *510*, 145516.
[13] S. Chaitoglou, R. Amade, E. Bertran, *Appl. Surf. Sci.* **2022**, *592*, 153327.
[14] S. Chaitoglou, Y. Ma, R. Ospina, G. Farid, J. Serafin, R. A. Rovira, E. Bertran-Serra, *ACS Appl. Nano Mater.* **2024**, *7*, 22631.
[15] B. Sukhbaatar, W. Qing, J. Seo, S. Yoon, B. Yoo, *Sci. Rep.* **2024**, *14*, 5850.
[16] S. Majumdar, S. Chaitoglou, J. Serafin, G. Farid, R. Ospina, Y. Ma, R. Amade-Rovira, E. Bertran-Serra, *Int. J. Hydrogen Energy* **2024**, *89*, 977.
[17] Y. Zhao, Y. Zhang, Y. Wang, D. Cao, X. Sun, H. Zhu, *Carbon Energy* **2021**, *3*, 895.
[18] A. Barranco, A. Borras, A. R. Gonzalez-Elipe, A. Palmero, *Prog. Mater. Sci.* **2016**, *76*, 59.
[19] F. Maillard, S. Schreier, M. Hanzlik, E. R. Savinova, S. Weinkauf, U. Stimming, *Phys. Chem. Chem. Phys.* **2005**, *7*, 385.
[20] S. Ghosh, G. Pagani, M. Righi, C. Hou, V. Russo, C. S. Casari, *J. Phys. D: Appl. Phys.* **2024**, *57*, 495305.
[21] B. Bayatsarmadi, Y. Zheng, V. Russo, L. Ge, C. S. Casari, S.-Z. Qiao, *Nanoscale* **2016**, *8*, 18507.
[22] S. Ghosh, M. Righi, A. Macrelli, D. Orecchia, A. Maffini, F. Goto, G. Bussetti, D. Dellasega, V. Russo, A. L. Bassi, C. S. Casari, *ChemSusChem* **2024**, *17*, e202400755.
[23] B. Bayatsarmadi, Y. Zheng, C. S. Casari, V. Russo, S.-Z. Qiao, *Chem. Commun.* **2016**, *52*, 11947.
[24] S. Chaitoglou, R. Ospina, Y. Ma, R. Amade, X. Vendrell, J. Rodriguez-Pereira, E. Bertran-Serra, *J. Alloys Compd.* **2024**, *972*, 172891.
[25] X. Zhang, C. Wang, B. C. F. Cheung, G. Mi, C. Wang, *J. Am. Ceram. Soc.* **2024**, *107*, 3724.
[26] S. Rodriguez-Miguel, Y. M. G. Farid, R. Amade, R. Ospina, J. L. Andujar, E. Bertran-Serra, S. Chaitoglou, *Heliyon* **2024**, *10*, e31230.
[27] B. Nayak, T. Dash, S. Pradhan, *J. Electron. Spectrosc. Relat. Phenom.* **2020**, *245*, 146993.
[28] S. E. Mrabet, M. Abad, C. Lopez-Cartes, D. Martínez-Martínez, J. Sanchez-Lopez, *Plasma Process. Polym.* **2009**, *6*, S444.
[29] Z. Li, L. Deng, I. Kinloch, R. Young, *Prog. Mater. Sci.* **2023**, *135*, 101089.
[30] J. Liu, W. Lv, Y. Mou, C. Chen, Y. Kang, *JMR&T* **2023**, *27*, 2490.
[31] D. J. Lim, N. A. Marks, M. R. Rowles, *Carbon* **2020**, *162*, 475.
[32] R. Hatel, M. Baitoul, *IOP Conf. Ser.: J. Phys.:Conf. Ser.* **2019**, *1292*, 012014.
[33] B. Gabhale, A. Jadhawar, A. Bhorde, S. Nair, H. Borate, R. Waykar, R. Aher, P. Sharma, A. Pawbake, S. Jadkar, *J. Nano- Electron. Phys.* **2018**, *10*, 03001.
[34] R. Balzer, V. Drago, W. Schreiner, L. F. D. Probst, *J. Braz. ChemSoc.* **2014**, *25*, 2026.
[35] M. Mizuno, Y. Sasaki, A. Yu, M. Inoue, *Langmuir* **2004**, *20*, 11305.
[36] J. Kang, J. Kim, M. Lee, Y. Son, D. Chung, S. Park, J. Jeong, J. Yoo, H. Shin, H. Choe, H. Park, Y. Sung, *Adv. Sci.* **2018**, *5*, 1700601.
[37] P. Krasovskii, O. Malinovskay, A. Samokhin, Y. Blagoveshchenskiy, V. Kazakov, A. Ashmarin, *Appl. Surf. Sci.* **2015**, *339*, 46.
[38] J. Song, S. Kwon, *ACS Appl. Mater. Interfaces* **2021**, *13*, 55611e20.
[39] S. Chaitoglou, R. Amade, R. Ospina, E. Bertran-Serra, *ACS Appl. Energy Mater.* **2023**, *6*, 6120.
[40] Y. Zhang, F. Gao, D. Wang, Z. Li, X. Wang, C. Wang, K. Zhang, Y. Du, *Coord. Chem. Rev.* **2023**, *475*, 214916.
[41] Z. Chen, X. Duan, W. Wei, S. Wang, B. Ni, *J. Mater. Chem. A* **2019**, *7*, 14971.
[42] Q. Ma, F. Cui, J. Zhang, T. Cui, *J. Colloid. Interface Sci.* **2023**, *629*, 649.
[43] Y. Ma, S. Chaitoglou, G. Farid, R. Amade, R. Ospina, A. Munoz-Rosas, E. Bertran-Serra, *Chem. Eng.* **2023**, *488*, 151135.
[44] R. Yao, K. Sun, K. Zhang, Y. Wu, Y. Du, Q. Zhao, G. Liu, C. Chen, Y. Sun, J. Li, *Nat. Commun.* **2024**, *15*, 2218.
[45] Y. Dang, L. Feng, W. Hu, W. Wang, Q. Zhang, B. Ma, *Int. J. Hydrogen Energy* **2021**, *46*, 39251.
[46] X. Deng, H. Chang, G. Zhang, *Int. J. Hydrogen Energy* **2022**, *47*, 902.
[47] F. Zhang, L. He, H. Pan, S. Lian, M. Wang, J. Yin, X. Chen, J. Ren, M. Chen, *Int. J. Hydrogen Energy* **2021**, *46*, 23615.

© 2025 The Author(s). Advanced Energy and Sustainability Research published by Wiley-VCH GmbH

26999412, 0, Downloaded from https://advanced.onlinelibrary.wiley.com/doi/10.1002/aesr.202500016 by CochraneItalia, Wiley Online Library on [25/08/2025]. See the Terms and Conditions (https://onlinelibrary.wiley.com/terms-and-conditions) on Wiley Online Library for rules of use; OA articles are governed by the applicable Creative Commons License